AGU PUBLICATIONS

JGR

Journal of Geophysical Research: Atmospheres

RESEARCH ARTICLE
10.1002/2016JD024748

Key Points:
- Traffic was the dominant rBC source in winter in Xi'an, followed by coal burning and biomass burning
- rBC size and mixing state were dependent on emission sources
- rBC was responsible for 45.7% of total aerosol direct radiative forcing at the surface

Supporting Information:
- Supporting Information S1

Correspondence to:
R.-J. Huang and J. Cao,
rujin.huang@ieecas.cn;
cao@loess.llqg.ac.cn

Citation:
Wang, Q., et al. (2016), Physicochemical characteristics of black carbon aerosol and its radiative impact in a polluted urban area of China, *J. Geophys. Res. Atmos.*, *121*, 12,505–12,519, doi:10.1002/2016JD024748.

Received 2 JAN 2016
Accepted 27 SEP 2016
Accepted article online 6 OCT 2016
Published online 24 OCT 2016

Physicochemical characteristics of black carbon aerosol and its radiative impact in a polluted urban area of China

Qiyuan Wang[1], Ru-Jin Huang[1,2,3], Zhuzi Zhao[1], Junji Cao[1,4], Haiyan Ni[1], Xuexi Tie[1], Shuyu Zhao[1], Xiaoli Su[1], Yongming Han[1,4], Zhenxing Shen[5], Yichen Wang[1], Ningning Zhang[1], Yaqing Zhou[1], and Joel C. Corbin[2]

[1]Key Laboratory of Aerosol Chemistry and Physics, Institute of Earth Environment, Chinese Academy of Sciences, Xi'an, China, [2]Laboratory of Atmospheric Chemistry, Paul Scherrer Institute, Villigen, Switzerland, [3]Centre for Atmospheric and Marine Sciences, Xiamen Huaxia University, Xiamen, China, [4]Institute of Global Environmental Change, Xi'an Jiaotong University, Xi'an, China, [5]Department of Environmental Sciences and Engineering, Xi'an Jiaotong University, Xi'an, China

Abstract Black carbon (BC) aerosol plays an important role in the Earth's radiative balance. An intensive measurement campaign was conducted at Xi'an, China, from December 2012 to January 2013 to investigate the sources and physicochemical characteristics of refractory BC (rBC) and its direct radiative forcing at the surface. The overall average rBC concentration for the campaign was $8.0 \pm 7.1\ \mu g\ m^{-3}$. Source apportionment based on positive matrix factorization showed that traffic was the dominant rBC source (46.0%), followed by coal burning (33.9%) and biomass burning (20.1%). The rBC mass size distributions were monomodal and lognormal with larger mass median diameters for coal burning source (215 nm) compared with the traffic source (189 nm). Coal burning rBC was more strongly associated with sulfate than traffic rBC, suggesting a higher cloud condensation nuclei activity. The slope of a robust linear regression between rBC and carbon monoxide (CO) for all samples was $5.9\ \mu g\ m^{-3}\ ppm^{-1}$, and the slope for the coal burning source ($4.5\ \mu g\ m^{-3}\ ppm^{-1}$) was larger than that for the traffic source ($2.7\ \mu g\ m^{-3}\ ppm^{-1}$). The net rBC emission during winter of 2009 was estimated to be 4.5 Gg based on the relationship between rBC and CO. A Tropospheric Ultraviolet and Visible radiation model showed that the average daytime value for the clear-sky direct radiative forcing due to rBC from 23 December 2012 to 31 January 2013 was $-47.7 \pm 28.9\ W\ m^{-2}$, which amounted to an average of 45.7% of the total surface atmospheric aerosol forcing.

1. Introduction

Rapid industrialization and urbanization in China in recent decades has led to a strong increase in air pollution [*Sheehan et al.*, 2014]. The severe haze observed in recent winters, for example, has received worldwide attention due to its effects on air quality, visibility, climate, and human health [e.g., *Tie and Cao*, 2009; *Cao et al.*, 2012a; *Huang et al.*, 2014]. An important component of this pollution is black carbon (BC), the light-absorbing, refractory material formed during the incomplete combustion of various fuels [*Bond et al.*, 2013]. The Fifth Assessment Report of the Intergovernmental Panel on Climate Change suggests that the direct radiative forcing (DRF) of BC ranks as the second most important contributor to anthropogenic radiative forcing, after CO_2, in the present-day atmosphere [*Intergovernmental Panel on Climate Change*, 2013]. The impacts of BC on the Earth's radiative balance may be far reaching and may include global dimming [*Wild et al.*, 2007], lower crop yields [*Shindell et al.*, 2012], and enhanced glacial melting [*Xu et al.*, 2009]. Furthermore, inhaled BC also can have adverse effect on human health [*Janssen et al.*, 2011].

China is one of the world's largest emitters of anthropogenic BC [*Zhang et al.*, 2009], and relatively high concentrations have been measured in Chinese cities. For example, *Cao et al.* [2007] investigated the concentrations of carbonaceous aerosols in $PM_{2.5}$ (particulate matter, PM, with aerodynamic diameters $\leq 2.5\ \mu m$) in 14 Chinese cities in 2003 using the Interagency Monitoring of PROtected Visual Environments (IMPROVE) analytical protocol and a commercial carbon analyzer. Their results showed that the average BC concentrations in the 14 cities were $9.9\ \mu g\ m^{-3}$ in winter and $3.6\ \mu g\ m^{-3}$ in summer. *Zhang et al.* [2008] used similar measurements to study PM_{10} (PM with aerodynamic diameters $\leq 10\ \mu m$) at 18 stations in China; their results showed annual mean BC concentrations of $0.35\ \mu g\ m^{-3}$ for remote background sites, $3.6\ \mu g\ m^{-3}$ for regional sites, and $11.2\ \mu g\ m^{-3}$ for urban sites. In addition to the nationwide BC studies, various projects have focused on local

and regional scales in China. For example, *Han et al*. [2009] reported that the annual average BC concentration in Beijing between 2005 and 2006, measured with a semicontinuous carbonaceous particle analyzer, was 6.9 $\mu g\,m^{-3}$. *Zhuang et al*. [2014] found that the annual mean BC concentration in Nanjing during 2012, measured with an aethalometer (optical-equivalent BC [*Petzold et al*., 2013]), was 4.2 $\mu g\,m^{-3}$. In the Pearl River Delta of China, *Wu et al*. [2013] measured ~12.3 $\mu g\,BC\,m^{-3}$ in the dry season and ~6.2 $\mu g\,BC\,m^{-3}$ in the rainy season. *Feng et al*. [2014] studied the seasonal variations of BC in Shanghai in 2011 and reported an annual average BC concentration of 3.3 $\mu g\,m^{-3}$.

The environmental and climate effects of the BC aerosol depend not only on the concentrations but also on the physical and chemical properties of the particles, especially their sizes and mixing state [*Bond et al*., 2013]. Although there have been numerous studies of BC in China as mentioned above, information on the size distributions and mixing state of BC is more limited than that for the total BC mass concentrations. Along these lines, cascade impactors have been used to collect size-segregated aerosol samples for BC analysis [*Cuccia et al*., 2013], and while that approach does provide useful information on the BC size and mass distributions, the time scales for the measurements are typically hours to days. This method relies on IMPROVE-like determination of BC (as elemental carbon or EC), which may lead to BC overestimation due to charring artifacts [*Cheng et al*., 2010; *Petzold et al*., 2013]. Such measurements also do not provide information on the BC mixing state.

Recently, an advanced online refractory BC (rBC) analyzer—the single-particle soot photometer (SP2; Droplet Measurement Technologies, Boulder, CO, USA)—has been used to measure the mass, size, and mixing state of rBC particles [*Schwarz et al*., 2006]. Because of the considerable expense and performance limitations of the SP2 [*Gysel et al*., 2012], there have been limited rBC studies in China that have made use of this technology [e.g., *Huang et al*., 2012a; *Wang et al*., 2015]. For the study presented here, we deployed an SP2, in combination with a variety of supporting instrumentation, during the winter in Xi'an, China, and we also made filter-based measurements of $PM_{2.5}$. The objectives of the study were (1) to estimate the contributions of various emission sources to the rBC aerosol mass and the impacts of sources on rBC size distribution and mixing state, (2) to characterize the relationship between rBC and carbon monoxide (CO) to calculate the relative emission factors, and (3) to evaluate the rBC effects on DRF at the surface. The results obtained with the SP2 contribute to our understanding of how rBC particle composition varies under different emission scenarios, and they may well lead to improvements in the parameterizations used in models of the rBC radiative effects.

2. Experimental Methods

2.1. Research Site

Xi'an, the largest city in Northwest China, is located on the Guanzhong Plain at the southern edge of the Loess Plateau, and it has a resident population of >8 million. Due to the rapid economic development, population growth, and urbanization over the past several decades, Xi'an often suffers from high loadings of $PM_{2.5}$, especially in wintertime [*Zhang et al*., 2011]. A 6 week intensive measurement program was conducted from 23 December 2012 to 31 January 2013, using samplers set up on the roof (~12 m above ground level) of the Institute of Earth Environment, Chinese Academy of Sciences, building (34.23°N, 108.88°E, supporting information Figure S1). This site is located in an urban zone [*Cao et al*., 2009], and it is surrounded by a residential/commercial area and is ~15 km southwest of downtown Xi'an.

2.2. Measurements

2.2.1. Online Measurements

The mass, size, and mixing state of individual rBC particles were determined with the use of an SP2, an instrument that analyzes single particles and whose detection principles have been described elsewhere [e.g., *Schwarz et al*., 2006; *Gao et al*., 2007]. Briefly, the SP2 uses a continuous intracavity Nd:YAG laser (1064 nm) with a Gaussian profile (TEM00 mode), and its power was measured by introducing monodisperse polystyrene latex spheres with nominal diameters of 269 nm into the instrument [*Schwarz et al*., 2010]. When an rBC-containing particle passes through the laser beam, the rBC core is heated to its incandescence temperature (~4000 K), and the resulting thermal radiation is measured by optical detectors as the particle vaporizes. The peak incandescence signal is linearly related to the rBC mass, and the detection method is not affected by the rBC mixing state or morphology for atmospheric particles [*Moteki and Kondo*, 2010]. Here the peak

intensity of the incandescence was calibrated to single-particle rBC mass using a standard fullerene soot sample (Lot F12S011, AlphaAesar, Inc., Ward Hill, Massachusetts) [*Laborde et al*., 2012]. A differential mobility analyzer (EPS-20 Electrical Particle Size, HCT Co. Ltd., Korea) was installed upstream of the SP2 (see Figure S2) to select monodisperse calibration particles over a mobility diameter range of 80–450 nm. This diameter range corresponds to particles with masses of ~0.3–25 fg, calculated when assuming the effective densities of *Gysel et al*. [2011]. The calibration for the peak intensity of the incandescence signal and the mass of fullerene soot were almost perfectly linear ($r = 0.9995$, $p < 0.0001$, not shown). As described below, we scaled the reported rBC values up by a factor of 1.1 to account for the fraction of rBC particles that were outside of the SP2 range of detection.

The capability of determining the mixing state of rBC is one of the major advantages of the SP2 measurements. The lag time between the scattering and incandescence signal peaks has been used as an indicator of the quantity of non-rBC components internally mixed with the individual rBC particles [*Moteki and Kondo*, 2007; *McMeeking et al*., 2011; *Wang et al*., 2014a]. This lag time occurs because rBC coatings vaporized before incandescent temperatures of the cores are reached, and the energy (time) required to vaporize rBC coatings thus delays the incandescent signal. We defined rBC particles as either thickly coated or uncoated/thinly coated according to the distribution of observed lag times, which was bimodal and had a local minimum at 2 μs (supporting information Figure S3). We defined the number fraction of thickly coated rBC particles (f_{BC}) as the proportion of particles with lag times longer than 2 μs. In the ambient atmosphere, f_{BC} typically is higher for more aged rBC particles due to the accumulation of coatings through condensation and coagulation. However, for inefficient combustion processes, freshly emitted rBC also may be thickly coated.

The mass concentrations of organics, sulfate, nitrate, and ammonium were measured with an aerosol chemical speciation monitor (ACSM, Aerodyne Research Inc., Billerica, MA), and the data were used to investigate the non-rBC materials on thickly coated rBC particles. Detailed descriptions of the operating principles and calibration procedures of the ACSM are available elsewhere [*Ng et al*., 2011]. Briefly, the ACSM focuses submicron particles (~40–1000 nm aerodynamic diameters) into a beam through an aerodynamic lens at a rate of 85 mL min^{-1} under vacuum. Then the nonrefractory material in the particle beam is vaporized on a hot surface (~600°C), ionized with 70 eV electrons, and finally analyzed with a quadrupole mass spectrometer. The chemically speciated, nonrefractory aerosol mass loadings are then extracted from the mass spectra. The ACSM response factor (RF) was calculated with the use of monodisperse 300 nm ammonium nitrate particles that were generated with an atomizer (Model 9302, TSI Inc., Shoreview, MN, USA) and a differential mobility analyzer (Model 3080, TSI Inc.). A range of ammonium nitrate concentrations from 0 to 25 μg m^{-3} was used for calculating the ACSM RF, which was produced by diluting the generated aerosol. The relative ionization efficiency for ammonium was directly determined from the ammonium nitrate calibration.

The columnar aerosol optical properties were measured during the daytime using a Cimel CE318-NE-type Sun-sky radiometer (Cimel Electronique, Paris, France). The radiometer makes direct spectral solar radiation measurements within a 1.2° full field of view at 340, 380, 440, 500, 675, 870, 940, 1020, and 1640 nm (nominal wavelength) nominally every 15 min. The direct Sun measurements were used to compute aerosol optical depths (AODs) at the various wavelengths expected for the 940 nm channel, which was used to obtain the column water vapor content. Single-scattering albedo (SSA) was retrieved from the sky radiance measurements in combination with the direct solar measurements of AOD at 440, 675, 870, and 1020 nm [*Dubovik et al*., 2000; *Li et al*., 2009]. The uncertainties for AOD and SSA are about 0.01–0.02 [*Eck et al*., 1999] and 0.03 [*Dubovik et al*., 2000], respectively. More detailed descriptions of the Sun-sky radiometer may be found in *Su et al*. [2014].

Five minute average mixing ratios for CO were obtained using gas filter correlation technology with infrared photometric detection. The CO analyzer (Model EC9830T, Ecotech Pty Ltd., Knoxfield, Australia) used for these analyses had a CO detection limit of 20 ppb. A standard CO gas (800 ppm) was diluted using a gas dilution calibrator (Model 4010 L, Sabio, USA) to produce a set of CO mixing ratios (e.g., 0.1, 2, 3, 4, and 5 ppm) used to calibrate the CO analyzer before and after the campaign. Hourly $PM_{2.5}$ loadings were determined with the use of an automatic Environmental Beta Attenuation Monitor (E-BAM, Met One Instruments, Inc., Grants Pass, OR, USA), which measured the attenuation of beta ray energy as the aerosol mass accumulated. The data for the planetary boundary layer (PBL) depth were obtained from the National Centers for Environmental

Prediction (NCEP, http://apps.ecmwf.int/datasets/). Relative humidity (RH) was measured every minute with the use of an automatic weather station (MAWS201, Vaisala, Vantaa, Finland) configured with an RH probe (Vaisala Model QMH101).

2.2.2. Offline Measurements

Sets of 24 h integrated $PM_{2.5}$ samples were collected using two battery-powered minivolume samplers (Airmetrics, Oregon, USA) that operated at a flow rate of 5 L min^{-1} and a high-volume air sampler (Tisch Environmental, Inc., USA) that had a flow rate of 1.05 m^3 min^{-1}. For the minivolume samplers (taken from 23 December 2012 to 25 January 2013), one set was collected on Teflon™ filters (47 mm, Whatman Limited, Maidstone, UK) for elemental analysis, and the other set was collected on quartz-fiber filters (47 mm, QM/A™; Whatman, Middlesex, UK) for water-soluble K^+ analysis. For the high-volume sampler (taken from 5 to 25 January 2013), the aerosols were collected on quartz-fiber filters (8 × 10 inches) for organic marker compound analysis.

The concentrations of a suite of elements, including S, Cl, Cr, Cu, Zn, As, Br, and Pb, were determined by energy-dispersive X-ray fluorescence (ED-XRF) spectrometry (Epsilon 5 ED-XRF, PANalytical B.V., the Netherlands) [*Xu et al*., 2012]. The Epsilon 5 spectrometer uses a three-dimensional polarizing geometry with 11 secondary targets (i.e., CeO_2, CsI, Ag, Mo, Zr, KBr, Ge, Zn, Fe, Ti, and Al) and one Barkla target (Al_2O_3), and configured this way, the instrument has a good signal-to-background ratio and low detection limits. The X-ray source is a side window X-ray tube with a gadolinium (Gd) anode, and the spectrometer operates at an accelerating voltage of 25–100 kV and a current of 0.5–24 mA (maximum power: 600 W). A germanium (Ge) detector (PAN 32) is used to detect the X-ray characteristic radiation. Each sample was analyzed for 30 min to acquire a spectrum of X-ray counts versus photon energies. The individual peak energies match specific elements, and the peak areas correspond to elemental concentrations.

A Dionex-600 ion chromatograph (IC, Dionex Inc., Sunnyvale, CA, USA) was used to determine the concentrations of water-soluble K^+. The instrument was equipped with a Dionex IonPacCS12A column, and 20 mM methanesulfonic acid was used as the eluent for the K^+ determinations. The detection limit was 10.0 mg L^{-1} for K^+. Standard reference materials produced by the National Research Center for Certified Reference Materials in China were analyzed for data quality assurance. More detailed descriptions of the ion chromatography analyses may be found in *Zhang et al*. [2011].

Organic marker compounds, including 17α(H)-21β(H) norhopane, picene, and levoglucosan, were measured using an in situ derivatization thermal-desorption gas chromatography time-of-flight mass spectrometric (IDTD–GC–TOF-MS) method [*Huang et al*., 2014]. Details of this method have been presented elsewhere [*Orasche et al*., 2011]. Briefly, punches of the sample filters were spiked with an internal standard mixture of isotopically labeled reference compounds to account for matrix effects. The punches were then placed in GC liners for an automated derivatization step, which used a liquid derivatization reagent N-methyl-N-trimethylsilyl-trifluoroacetamide (MSTFA, Macherey-Nagel, Germany). During 16 min of desorption, MSTFA was added to the carrier gas to quantitatively silylate polar organic compounds and optimize the desorption process. Derivatized and desorbed molecules were first trapped on a precolumn before separation by gas chromatography (Agilent 6890 GC, equipped with a BPX-5 capillary column, SGE, Australia). Finally, the detection and quantification of selected compounds were carried out with the use of a Pegasus III time-of-flight mass spectrometer (TOF-MS) using the Chroma TOF software package (LECO, St. Joseph, MI, USA).

2.3. Receptor Model Source Apportionment

Positive matrix factorization (PMF) [*Paatero and Tapper*, 1994], which has been widely used in source apportionment studies [e.g., *Cao et al*., 2012b; *Wang et al*., 2013; *Xiao et al*., 2014], was used to evaluate the relative contributions of different emission sources to the rBC aerosol mass. Briefly, the PMF model assumes that the concentrations of the species at receptor site can be represented as linear combinations of various sources; these sources are termed "factors" in the model. The model decomposes the concentrations at the receptor site into three matrices, which are the contributions (G), factor profiles (F), and residuals (E):

$$X_{ij} = \sum_{k=1}^{p} G_{ik} F_{kj} + E_{ij} \quad (1)$$

where X_{ij} represents the ambient concentrations of the jth species on the ith day, G_{ik} is the factor contribution of k source on the day i, F_{kj} is source profile of species j in the kth source, and E_{ij} represents the ($i \times j$) matrix of

fit residuals. These matrices are obtained by minimizing the object function Q, based on a constrained, weighted least squares. The Q function is defined as follows:

$$Q = \sum_{i=1}^{n} \sum_{j=1}^{m} \left(\frac{x_{ij} - \sum_{k=1}^{p} G_{ik} F_{kj}}{U_{ij}} \right)^2 \quad (2)$$

where U_{ij} is an estimation of the uncertainty in species j measured on the day i.

For this study, the daily data for the $PM_{2.5}$ chemical species and their associated uncertainties were used as the input data for the PMF analysis following the procedure of *Polissar et al*. [1998]. As PMF is a descriptive model, there are no objective criteria for choosing the optimum number of factors that should be retained for discussion [*Chen et al*., 2010]. For our study, a three-factor solution was retained as offering the best interpretability. Examination of the frequency distribution of the scaled residuals, which were mostly concentrated between −2 and +2 (see Figure S4), indicated a good fit between the PMF model results and the input data. The factor profiles and the daily contributions of each factor were determined by the PMF model, and after those results were obtained, a multiple linear regression analysis was used to calculate the contribution of each extracted factor (source) to the rBC mass concentrations. This two-step approach was taken to avoid the issues that may arise in PMF when combining different numbers of variables from different measurement techniques [*Slowik et al*., 2010].

2.4. DRF Calculation

A Tropospheric Ultraviolet and Visible (TUV) radiation model [*Madronich*, 1993], using a total of 140 wavelength bands from 180 to 730 nm, was used to estimate the direct aerosol radiative forcing at the local Earth's surface. Key input parameters to this model are the AOD and SSA, which reflect the aerosol column burden and composition. In our study, these two values were retrieved from the Sun-sky radiometer measurements. The surface albedo is another influential factor, and it was derived from measurements made with the Moderate Resolution Imaging Spectroradiometer.

The Optical Properties of Aerosols and Clouds (OPACs) model can provide optical properties of aerosols in the solar and terrestrial range [*Hess et al*., 1998]. The data set in OPAC contains the microphysical and optical properties for six types of water clouds, three ice clouds, and 10 aerosol components. In this way, the OPAC was used to derive the rBC optical depth by adopting urban aerosol type. The measured rBC volume-equivalent radius (section 3.2) and number concentration were used. The rBC refractive index was set to 1.95–0.79i [*Bond and Bergstrom*, 2006]. The density of rBC was assumed to be 2.0 g cm^{-3} [*Slowik et al*., 2004]. The modeled rBC absorption coefficient was used to calculate the rBC optical depth on the base of exponential aerosol height profiles ($N(h)$), which is defined as follows [*Hess et al*., 1998]:

$$N(h) = N(0)e^{-\frac{h}{Z}} \quad (3)$$

where $N(0)$ is the number concentration of rBC at the surface layer and h and Z are the altitude above ground in kilometers and the scale height in kilometers, respectively. The same exponential function in OPAC was used to estimate the aerosol vertical profile, but with appropriate PBL depth obtained from NCEP. The uncertainty in the estimation of the rBC optical depth was ~30%, derived from the uncertainty of the rBC measurements (~25%) [*Wang et al*., 2014b].

In this way, wavelength-dependent aerosol optical properties for the total aerosol and for rBC particles alone were separately used as the original default values in TUV model for Xi'an. Radiative fluxes at the surface were calculated as a function of the solar zenith angle. Cloud cover was not considered here because the AOD and SSA data were obtained only under clear-sky conditions. The uncertainty in the rBC DRF at the surface determination was ~35%, which was estimated from the square root of uncertainties caused by AOD (~10%), SSA (~15%), and rBC optical depth (~30%). The DRF of total aerosols (or rBC) at the surface is defined as the difference between the net shortwave radiative flux with and without aerosol as follows:

$$\mathrm{DRF}_{\mathrm{surface}} = \mathrm{Flux\ (net)}_{\mathrm{with\ aerosol\ (or\ rBC),\ surface}} - \mathrm{Flux\ (net)}_{\mathrm{without\ aerosol\ (or\ rBC),\ surface}} \quad (4)$$

Table 1. Refractory Black Carbon (rBC) Concentration, $PM_{2.5}$ Concentration, CO Mixing Ratio, and Planetary Boundary Layer (PBL) Depth for the Entire Sampling Campaign Period and on Weekdays and Weekends[a]

Period	rBC ($\mu g\,m^{-3}$)	$PM_{2.5}$ ($\mu g\,m^{-3}$)	CO (ppm)	PBL (m)
Weekdays	7.4 ± 5.7	195.9 ± 120.1	1.6 ± 0.9	449.9 ± 378.3
Weekends	9.4 ± 7.8	177.6 ± 133.9	1.8 ± 1.3	371.1 ± 370.5
Total average	8.0 ± 7.1	191.2 ± 124.0	1.7 ± 1.0	410.6 ± 362.1

[a]All values are mean ± standard deviation.

3. Results and Discussion

3.1. rBC Concentrations and Sources

A time series plot of the hourly averaged rBC mass concentrations for the entire campaign period is shown in Figure S5, and a statistical summary of the data is presented in Table 1. The rBC concentrations exhibited clear "sawtoothed" patterns, likely due to the day-to-day variations in atmospheric mixing conditions and advective transport. The overall mean for the rBC aerosol (± standard deviation, SD) was 8.0 ± 7.1 $\mu g\,m^{-3}$, and the concentrations ranged from 0.2 to 38.8 $\mu g\,m^{-3}$. The maximum rBC value occurred around midnight on 16 January 2013, which was possibly attributed to the low PBL depth at that time leading to the accumulation of pollutants. The average mass concentration of rBC during weekdays (7.4 ± 5.7 $\mu g\,m^{-3}$) was ~30% lower than that during weekend (9.4 ± 7.8 $\mu g\,m^{-3}$) periods, and this was most likely due to the slightly greater depth of the PBL during weekdays (Table 1). Compared with previous studies, the average rBC at Xi'an was higher than what was observed with the SP2 at other Chinese cities, including 5.5 $\mu g\,m^{-3}$ at Beijing [*Wu et al.*, 2016], 4.1 $\mu g\,m^{-3}$ at Shenzhen [*Huang et al.*, 2012a], 2.0 $\mu g\,m^{-3}$ at Shanghai [*Huang et al.*, 2012b], and 7.1 $\mu g\,m^{-3}$ at Jiaxing [*Huang et al.*, 2013].

Figure 1 shows the diurnal variations of rBC for the entire study: the mean and median rBC concentrations exhibited similar diurnal patterns, with "two peaks and two valleys" each day. The median rBC concentrations reached a peak value (6.6–7.6 $\mu g\,m^{-3}$) in the morning around 07:00–09:00 local standard time (LST), followed by a slow decrease to a minimum (2.5–3.5 $\mu g\,m^{-3}$) in the afternoon around 14:00–17:00. The rBC concentrations then increased to secondary peak values (9.4–11.0 $\mu g\,m^{-3}$) at night around 22:00–01:00 and again slowly decreased to a minimum (~6.5 $\mu g\,m^{-3}$) in the early morning around 05:00. The diurnal cycle can be explained by variations in local anthropogenic activities and hence emissions, transport, and the dynamics of the PBL. The peak rBC concentrations in the morning were likely caused by rush hour traffic and low PBL depths which led to the near-surface accumulation of pollutants. With an increase in solar heating as the day progressed, deeper and more turbulent PBLs formed and that in turn led to increased vertical transport and dilution of pollutants. The increase in rBC values at night can be explained by the development of a shallow and

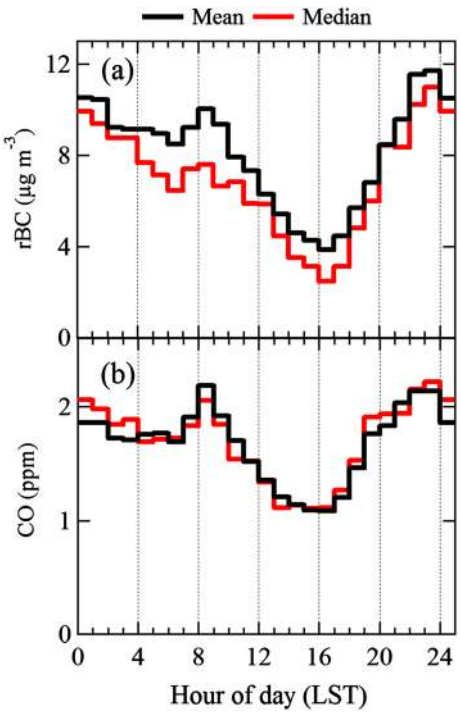

Figure 1. Diurnal variations (local standard time, LST) of the (a) rBC mass concentrations and (b) CO mixing ratios averaged over the entire campaign.

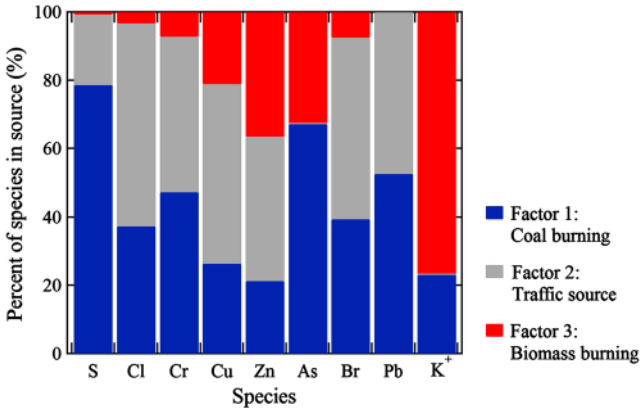

Figure 2. Source profiles for the three sources identified by the positive matrix factorization (PMF) model.

stable PBL due to nocturnal radiative cooling and enhanced rBC emissions from evening rush hour traffic as well as coal and biomass burning for domestic heating. Figure S6a shows that the weekdays and weekends exhibited similar diurnal variations, with the largest difference in the morning, especially during the rush hour traffic period. As the total numbers of motor vehicles between these two periods were similar (Figure S6c), this difference in the morning was likely due to the shallower PBL during weekends compared with weekdays (Figure S6b).

To estimate the contributions of different sources to rBC mass concentrations, PMF modeling was performed using the measured K^+ and elemental (S, Cl, Cr, Cu, Zn, As, Br, and Pb) concentrations as model inputs. Three sources were identified, namely, coal burning, traffic, and biomass burning, and the three source profiles are shown in Figure 2. Factor 1 had high loadings of S, As, Pb, and Cr, and it was identified as coal burning because these elements are typically enriched in coal fly ash [*Tian et al*., 2014]. Factor 2 was characterized by high loadings of Br, Cu, Zn, Cl, and Pb, and it was considered to represent a traffic source because these elements are typically emitted by motor vehicles [*Zechmeister et al*., 2005]. Factor 3, biomass burning, was characterized by a strong loading of K^+, a water-soluble ion known to be heavily enriched in emissions from biomass burning [*Cheng et al*., 2013].

A multiple linear regression analysis was then used to calculate the contribution of each of the three factors to the rBC mass concentrations. Good agreement ($r = 0.93$, slope = 0.97) was obtained between modeled and measured rBC concentrations (see scatterplot in Figure S7) providing support for the model's performance. To further evaluate the validity of the PMF-resolved source contributions, we compared the rBC concentrations calculated for each of the three sources with chemical markers of those presumptive sources. These markers were 17α(H)-21β(H) norhopane, picene, and levoglucosan, which were used to represent vehicular emissions [*Huang et al*., 2014], coal burning [*Rutter et al*., 2009], and biomass burning [*Zhang et al*., 2014], respectively. Supporting information Figure S8 shows a strong correlation ($r = 0.77$) between traffic rBC and 17α(H)-21β(H)norhopane, while coal burning and biomass burning rBC showed moderate correlations with picene ($r = 0.60$) and levoglucosan ($r = 0.62$). These relationships indicate that the PMF results provide a reasonable representation of the rBC sources and concentrations during the winter at Xi'an.

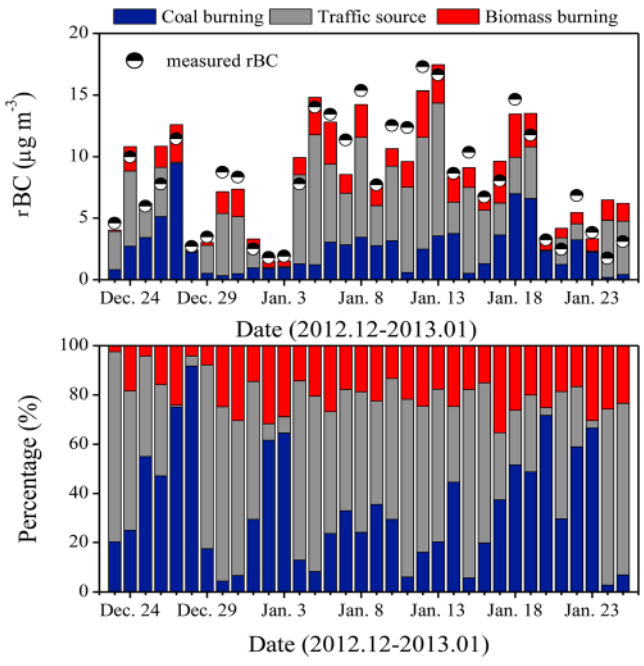

Figure 3. Daily variations of the contribution of each PMF-resolved source to the rBC loadings for the entire campaign period.

Time series plots for the three sources are shown in Figure 3. The traffic

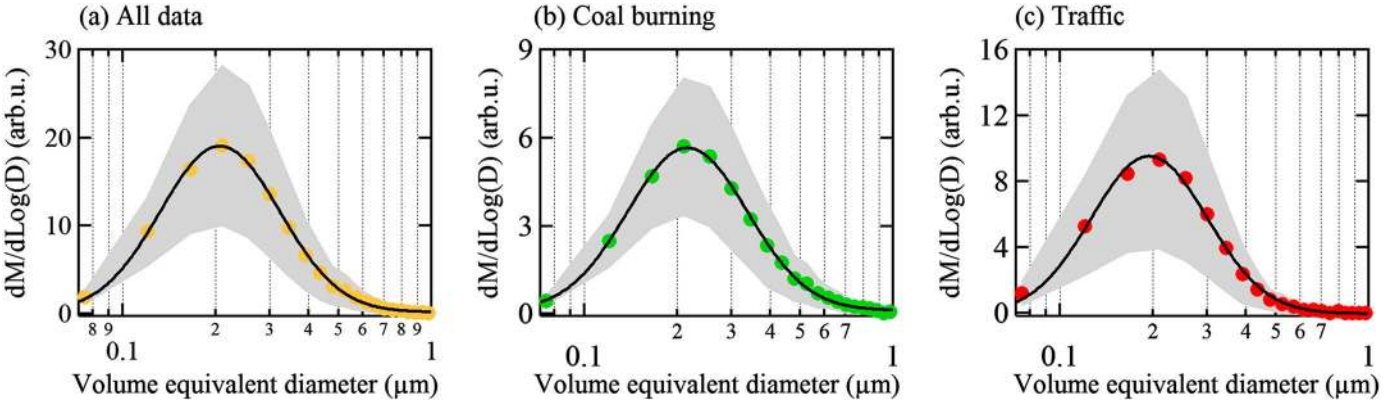

Figure 4. Mass size distributions of rBC in volume-equivalent diameters for (a) the entire sampling campaign and (b) the coal burning and (c) traffic sources, respectively. A biomass burning size distribution could not be obtained, as described in the text. The solid lines represent lognormal fits. The grey shadow corresponds to the standard deviations. In the vertical labels "M" and "D" denote rBC mass and void-free equivalent diameters (assuming 2 g cm^{-3} density), respectively, and "arb. u." stands for arbitrary units.

source was the largest contributor, accounting for 0.8 to 77.2% of the total rBC and averaging 46.0 ± 25.1%. The average percent contribution for coal burning was 33.9 ± 23.8% (± SD) of the rBC mass, and it ranged from 2.8 to 91.7%. The biomass burning source contributed 20.1 ± 7.9% of the rBC mass and ranged from 2.5 to 35.3%. It should be noted that the contribution of each source as represented by the PMF model resulted from a combination of local emissions and transport influences. Over short time scales, such as the length of our study, the emission sources can be considered relatively stable, and if one makes that assumption, it would be reasonable to conclude that the variations in source contribution were most likely due to differences in the dynamics of the PBL, variations in wind speed, and advection, all of which can affect the dispersal of rBC particles. Our results are generally consistent with those of *Zhang et al.* [2015] who measured ^{14}C in BC fractions during extreme winter-haze episodes in Xi'an in January 2013 and found that fossil emissions (e.g., coal combustion and vehicle exhaust) were the main (75%) sources for BC, while the remaining 25% was from biomass burning.

3.2. rBC Size Distributions and Mixing State as Influenced by Different Sources

Absorption calculations in radiative transfer models require information on the size distributions of rBC particles and coatings on them [*Bond et al.*, 2013], and therefore, understanding what causes the differences in sizes and mixing states of rBC particles is critical for developing better climate models. Figure 4a shows the mass size distributions of rBC observed for the entire campaign. It is noteworthy that the rBC sizes as presented are the mass-equivalent diameters of the rBC cores only, and they do not include the contributions from internally mixed non-rBC material. A monomodal lognormal function fits the data well for rBC particles between 70 and 1000 nm in diameter, and this is consistent with previous observations [*Schwarz et al.*, 2006; *Shiraiwa et al.*, 2007; *Subramanian et al.*, 2010]. The lognormal fit provides an indication of the fraction of submicron mass that was outside the SP2 measurement range. To account for the missing mass, the difference between the area under the monomodal lognormal fit and the measured rBC mass was used to scale up the rBC mass concentrations as noted in the measurements section; this resulted in an adjustment of a factor of 1.1.

As shown in Figure 4a, the mass median diameters (MMD ± SD) and geometric standard deviations (σ_{gc}) derived from the monomodal lognormal fitting of the data were 207 ± 2 nm and 1.56, respectively. These values represent populations of both internally and externally mixed rBC particles, which evidently derive mainly from motor vehicles, coal burning, and biomass burning in Xi'an and surrounding areas. This MMD value is within the range of 150–230 nm reported in previous SP2 studies [*Huang et al.*, 2012a, and references therein]. To estimate the MMD corresponding to each source in Figure 3, we selected periods where each source accounted for over 70% of the total rBC mass concentration and assumed—as a first approximation—that to be the only source contributing to the rBC aerosol population for that particular day. Only the traffic and coal burning sources could be characterized in this way because none of the biomass burning data met

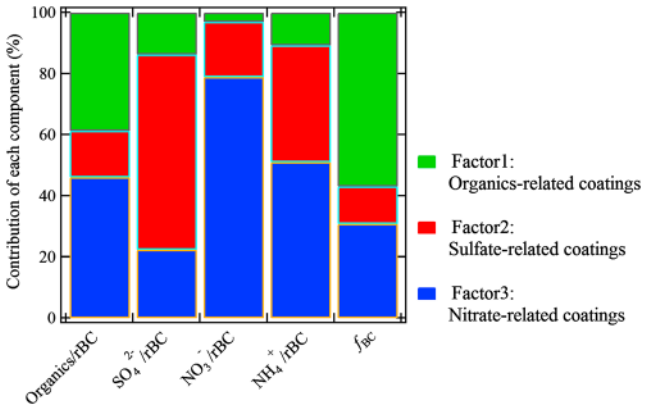

Figure 5. Contributions of organics/rBC, SO_4^{2-}/rBC, NO_3^-/rBC, NH_4^+/rBC, and f_{BC} in the three-factor model.

this criterion. To further reduce the influences from other sources, we only used the data for the traffic source for the morning and evening rush hours (07:00–09:00 and 17:00–19:00 LST, respectively), while the data from coal burning were used for the other parts of the day.

Figures 4b and 4c show the monomodal lognormal fits of rBC mass size distributions from these two sources. The MMD of coal burning was 215 ± 2 nm with $\sigma_{gc} = 1.56$, which is ~26 nm larger than the MMD of traffic source (189 ± 1 nm and $\sigma_{gc} = 1.55$). Dissimilar size distributions of rBC particles from the two sources can be explained by differences in both the fuels and combustion conditions. For example, *Schwarz et al*. [2008] found that the rBC MMD for particles from a biomass burning plume (210 nm) was larger than that from urban fossil fuel burning (170 nm). *Liu et al*. [2014] reported that rBC particles from motor vehicles have smaller MMDs compared with those from solid fuel burning. Although different mass size distributions of rBC particles have been reported for specific sources, to the best of our knowledge, the present study is the first in China to show larger rBC MMDs for ambient aerosols from coal burning compared with those from a roadway source. This limited observation may be likely due to the lack of high time resolution of rBC measurements (e.g., SP2) to capture the coal burning episodes in the atmosphere.

The difference in the rBC mixing state (expressed as f_{BC}) between the traffic and coal burning sources was also investigated. The average f_{BC} for the traffic source was 36.9 ± 7.2%, which indicates that fresh, uncoated or thinly coated rBC particles composed the bulk of the rBC aerosol from the roadway source. Compared with the traffic source, the f_{BC} for the coal burning source was nearly 40% higher, with an average value of 50.3 ± 7.7%, suggesting considerable mixing and aging of the aerosol or that more heavily coated rBC particles were produced by coal burning.

The PMF model was also used to evaluate the potential contributions of organics, sulfate, nitrate, and ammonium to the coatings on rBC particles [*Shiraiwa et al*., 2007; *Metcalf et al*., 2012; *Wang et al*., 2014b]. The input parameters for the model used here were the ratios of the mass concentrations of organics, SO_4^{2-}, NO_3^-, and NH_4^+, measured by ACSM to the corresponding rBC loadings and f_{BC} values. Mass ratios instead of absolute mass concentrations of each species were used as inputs because they can provide a better representation of the relative amounts of materials coating the rBC particles [*Shiraiwa et al*., 2007]. The PMF model was run multiple times, and the three-factor solution was retained as having the most physically interpretable profiles (Figure 5). The parameters predicted by the PMF model, including f_{BC} and the ratios of organics/rBC, SO_4^{2-}/rBC, NO_3^-/rBC, and NH_4^+/rBC, agreed well with the observed values and had correlation coefficients of 0.91, 0.85, 0.96, 0.95, and 0.97, respectively. As shown in Figure 5, Factor 1 was characterized by the highest contribution of organics/rBC and f_{BC} indicating that organic compounds were the main contributor to this coating-related factor. Factor 2 was dominated by SO_4^{2-}/rBC, suggesting that sulfate was the major contributor to the coatings associated with this factor. Factor 3 is most heavily loaded with NO_3^-/rBC, and therefore, nitrate was likely the major contributor to rBC coatings from this factor.

A multiple linear regression analysis was then used to calculate the real-time contribution of each of the three coating factors in Figure 5 to f_{BC}. Traffic and coal burning episodes based on the classification criteria of rBC mass as discussed in section 3.1 were selected to investigate the contributions of each coating factor to f_{BC}. Figure 6 shows that the inferred contributions of organics, sulfate, and nitrate to the coatings on the coal burning rBC were 44.0%, 32.3%, and 23.7%, respectively. In comparison, the inferred contribution of organics to the coatings on traffic-related rBC was higher, at 63.2%, while the sulfate contribution was lower, at 10.3%. The proportion of nitrate (26.5%) in rBC coatings was similar for the two groups. The differences in the

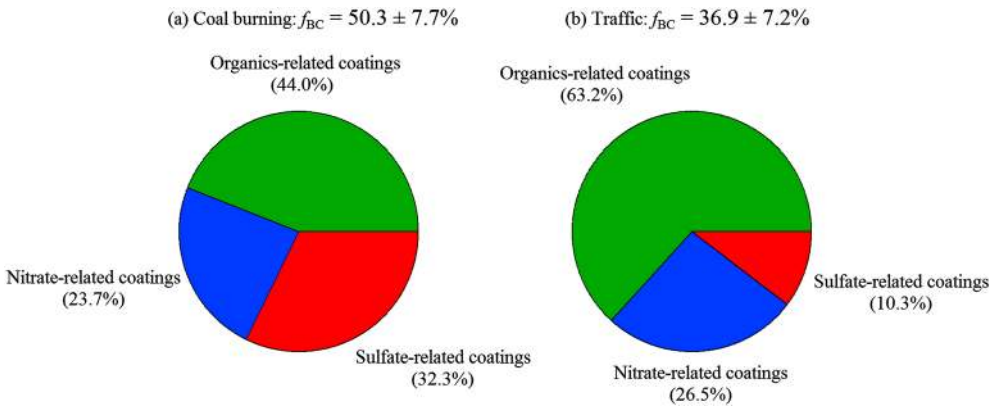

Figure 6. Contributions of organics-, sulfate-, and nitrate-related coatings to the number fraction of thickly coated rBC (f_{BC}) particles associated with the (a) coal burning and (b) traffic sources.

apparent importance of organics and sulfate as coatings were likely influenced by the history of these rBC particles through condensation, coagulation, and photochemical oxidation after emission by motor vehicles and coal burning. In addition, differences between the combustion sources may also have influenced the rBC coatings. That is, the rBC particles in the traffic sample group were mainly produced by internal combustion engines along with some coemitted organics from incomplete combustion; coal on the other hand contains a substantial amount of sulfur which after combustion ends up as sulfate [*Moffet and Prather*, 2009]. However, based on the high percentage of nitrate in both cases, we believe that potentially rapid photochemical aging must have played an important role.

Our observations imply that coal burning rBC particles should more readily act as cloud condensation nuclei than the roadway rBC particles. That is, one would expect that the enhanced coatings of water-soluble ions on the coal-derived rBC would render those particles more hygroscopic. As a result, the PM from coal combustion with these coatings may be a stronger contributor to the first indirect effect of the aerosol at low altitudes than the particles produced by motor vehicles. On the other hand, the average lifetime of coal burning rBC particles could be shorter than that of the traffic rBC particles due to the more efficient wet removal of the more hygroscopic particles combined with the faster sedimentation of larger particles.

3.3. Relationship Between rBC and CO

A time series plot (Figure S5) shows large variability in the CO mixing ratios, which ranged from 0.16 to 5.64 ppm and had a mean (± SD) of 1.7 ± 1.0 ppm (Table 1). Similar to the diurnal pattern shown for rBC mass (Figure 1), the CO mixing ratio showed high values in the early morning and at night and small values in the afternoon. As both substances are produced by the incomplete combustion of carbonaceous fuels, one might expect the CO mixing ratios to correlate well with the rBC concentrations. However, the balance between these two species is affected by the emission sources, especially type of fuels burned and combustion efficiencies, and therefore, the rBC/CO ratio varies with the contributions from specific sources, and it can be used to evaluate their impacts under some circumstances [*Spackman et al*., 2008]. As the atmospheric lifetime of CO is much longer than that of rBC, the interpretation of rBC/CO ratios is most meaningful after correcting the CO data for the background [*Kondo et al*., 2006]. In this study, the background CO mixing ratio was estimated to be ~0.19 ppm based on the lowest 1.25th percentile of the CO values during the sampling period, following *Kondo et al*. [2006]. Only the background-corrected CO (ΔCO) values >0.02 ppm were used for the comparisons with the rBC loadings in order to limit the influence of low ΔCO values.

The relationship between rBC and ΔCO was investigated by performing a robust linear regression [*Miconnet et al*., 2005] of the rBC mass concentrations versus the ΔCO mixing ratios (Figure 7). A relatively tight correlation was found between rBC and ΔCO ($r = 0.83$), which suggests that these two substances were probably controlled by common or proximate sources. The slope (as rBC/ΔCO) of the regression line shown in Figure 7a was 5.9 $\mu g\, m^{-3}\, ppm^{-1}$, and this was arguably representative of the mixture of sources that influenced in the wintertime atmosphere at Xi'an. Compared with previous studies, the rBC/ΔCO ratio at Xi'an was higher than at Beijing (3.5 to 5.8 $\mu g\, m^{-3}\, ppm^{-1}$) [*Han et al*., 2009] and Guangzhou

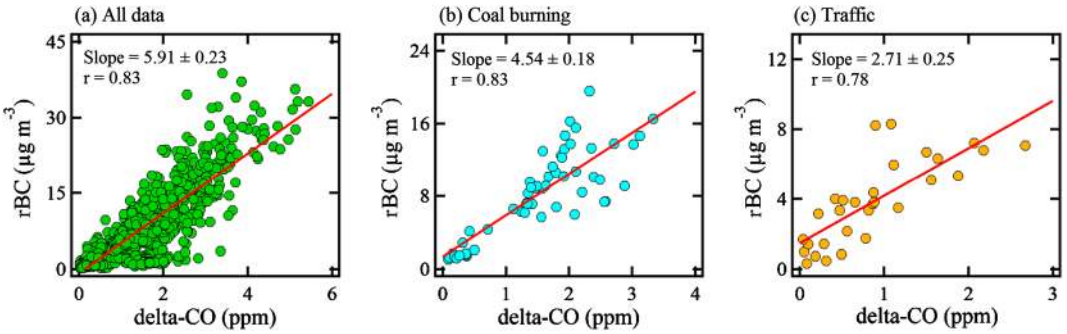

Figure 7. Scatterplot of rBC concentrations versus CO mixing ratios for (a) the entire campaign and for the (b) coal burning and (c) traffic sources, respectively. Each data point is an hourly average. The red line fits were calculated by robust linear regression.

(4.5 $\mu g\,m^{-3}\,ppm^{-1}$) [*Verma et al.*, 2010], China, Tokyo (5.7 $\mu g\,m^{-3}\,ppm^{-1}$) [*Kondo et al.*, 2006], Japan, Mexico City (1.0 $\mu g\,m^{-3}\,ppm^{-1}$) [*Baumgardner et al.*, 2007], and within the range of 0.8–6.2 $\mu g\,m^{-3}\,ppm^{-1}$ measured in the boundary layer over Europe [*McMeeking et al.*, 2010].

It is unlikely that the differences rBC/ΔCO ratios at the various sites listed above were solely due to the different methods used to measure BC-containing particles—even though this is an issue—but instead, they are almost certainly affected by the types of combustion and burning conditions. Along these lines, the rBC/ΔCO ratios in our study differed when the data were separated by source as described above. As shown in Figures 7b and 7c, the rBC/ΔCO ratio associated with coal burning (4.5 $\mu g\,m^{-3}\,ppm^{-1}$) was larger than that for the traffic source (2.7 $\mu g\,m^{-3}\,ppm^{-1}$). Interestingly, the coal burning and traffic-related rBC/ΔCO ratios were both lower than the average value for the entire campaign, which suggests that other emission sources had large rBC/ΔCO ratios. One of those sources is most likely biomass burning, which has indeed been found to have high rBC/ΔCO ratios [*Spackman et al.*, 2008].

In addition to the variations in rBC and CO produced by the different sources, the balance between them also can be affected by the physical and chemical processes that act to destroy or remove them from the atmosphere. For instance, the primary removal mechanism of CO is oxidation by the hydroxyl radical, which leads to the formation of CO_2 and imposes a CO lifetime of ~1 month [*Dickerson et al.*, 2002]. In comparison, BC-containing particles are much more refractory and are mainly removed by physical processes—namely, wet and dry deposition; they have a lifetime of a few days to weeks [*Bond et al.*, 2013]. Supporting information Figure S9 shows the relationship between the rBC/ΔCO ratios and RH. A regression of rBC/ΔCO versus RH showed a strong negative relationship ($r = -0.98$), suggesting stronger dry deposition of rBC at higher RH. Future work will aim to understand the mechanism behind this relationship. From the slope of the regression, one can calculate an apparent loss rate for rBC versus RH of 0.045 $\mu g\,m^{-3}\,ppm^{-1}\,RH\,(\%)^{-1}$.

Previous studies have shown that when direct measurements are not available, BC emissions can be reliably estimated using an empirically derived relationship to CO [*Kondo et al.*, 2006; *Baumgardner et al.*, 2007]. Following this procedure, we calculated the rBC emissions based on the strong linear relationship between rBC and CO. The emission of CO for the Xi'an metropolitan area (34.07°N–34.43°N, 108.78°E–109.22°E) for the winter of 2009 (defined as January, February, and December) has been estimated to be 958 Gg (Q. Zhang, Tsinghua University, personal communication, 2013). Based on the linear regression model (Figure 7a), the corresponding integrated emission of rBC over winter of 2009 would be 4.5 Gg.

3.4. Effect of rBC on DRF at the Earth's Surface

Aerosol radiative forcing is the perturbation of the Earth atmosphere system due to the scattering and absorption of radiant energy by aerosols. Here the DRF for the total aerosol condition and the rBC-only condition were estimated at surface using the TUV model as described in section 2.4. Figure 8a shows average daytime values for the clear-sky total aerosol DRF at the surface. The average daytime total aerosol DRF value was $-100.5 \pm 46.1\,W\,m^{-2}$ and ranged from -231.6 to $-28.3\,W\,m^{-2}$. These negative surface DRF values imply a net cooling effect of the aerosol. Compared with previous DRF studies in the ultraviolet and visible region in

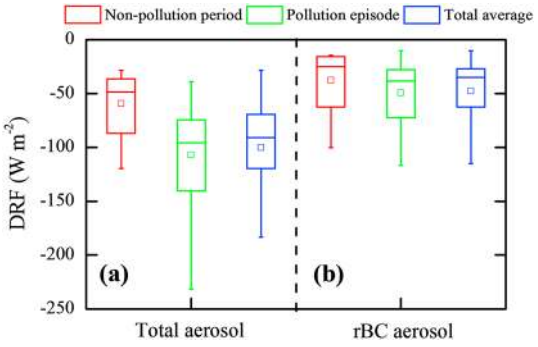

Figure 8. Box and whisker plot of the direct radiative forcing (DRF) at surface due to total aerosol and rBC during polluted and nonpolluted periods. The squares inside the boxes are the mean values, the horizontal lines in the boxes are the medians, the lower and upper limits of the boxes are the 25th and 75th percentiles, and the vertical lines extend to 5th and 95th percentiles.

China, the average DRF value at Xi'an was more negative than Nanjing ($-39.4\,W\,m^{-2}$) [*Zhuang et al.*, 2014], Linan ($-73.5\,W\,m^{-2}$) [*Xu et al.*, 2003], Xianghe ($-16.6\,W\,m^{-2}$) [*Xia et al.*, 2007a], and Taihu ($-17.8\,W\,m^{-2}$) [*Xia et al.*, 2007b].

According to the China National Ambient Air Quality Grade II Standard (GB3095-2012), the ambient air quality is classified as a "pollution period" if the $PM_{2.5}$ mass concentration exceeds $75\,\mu g\,m^{-3}$; otherwise, it is defined as a "nonpollution period," and we stratified our data using this standard. The average daytime total aerosol DRF during pollution periods was stronger than that during nonpollution periods by a factor of ~2 (-107.4 versus $-59.3\,W\,m^{-2}$), indicating stronger cooling during polluted periods. This can be explained by the much larger $PM_{2.5}$ loadings during pollution episodes ($238\,\mu g\,m^{-3}$) compared with nonpolluted periods ($33\,\mu g\,m^{-3}$), and this analysis clearly shows that air pollution can lead to a reduction in surface-reaching radiation as a result of light scattering and absorption by the aerosol.

Figure 8b also shows the mean daytime values for clear-sky rBC DRF at the surface for the entire campaign as well as for the pollution and nonpollution periods. The average daytime rBC DRF during the study ranged from -116.8 to $-10.3\,W\,m^{-2}$, with an average value of $-47.7 \pm 28.9\,W\,m^{-2}$; this contributed $45.7 \pm 12.2\%$ of total aerosol surface DRF. As these calculations were constrained by the Sun-sky radiometer measurements, they indicate that even though the concentration of rBC accounted to only ~4.2% of the $PM_{2.5}$ loading (see Table 1), its contribution to the aerosol forcing was disproportionately large due to its strong light absorption properties. The average daytime rBC DRF was $-49.3\,W\,m^{-2}$ for pollution periods compared with $-37.8\,W\,m^{-2}$ for nonpollution periods. It is noteworthy that the contribution of rBC DRF to the total aerosol DRF was lower during pollution periods (43.7%) than in nonpollution periods (57.9%). That is, even though the mass concentration of rBC was ~7 times higher during pollution periods compared with nonpollution periods (10.0 and $1.4\,\mu g\,m^{-3}$, respectively), the rBC mass fraction of $PM_{2.5}$ was comparable during these two periods (~4.2%). Thus, scattering by aerosol particles was more important, relative to absorption, during pollution periods than during nonpollution periods.

4. Summary and Conclusions

We made a comprehensive set of measurements to characterize the wintertime refractory black carbon (rBC) aerosol in Xi'an, the largest city in northwestern China. The mass, size, and mixing state of rBC particles were measured with a single-particle soot photometer (SP2). Colocated filter-based measurements of $PM_{2.5}$ chemical species and online CO gas measurements were used to investigate the sources of the rBC aerosol. A Tropospheric Ultraviolet and Visible radiation model combined with optical properties of aerosols measured with a Sun-sky radiometer was used to calculate the rBC direct radiative forcing at the Earth's surface. The average mass concentration of rBC was $8.0 \pm 7.1\,\mu g\,m^{-3}$, with high values in the morning and at night and lower values in the afternoon. Receptor modeling showed that motor vehicle traffic was the largest contributor to the rBC aerosol, accounting for $46.0 \pm 25.1\%$ of the total rBC, followed by coal burning ($33.9 \pm 23.8\%$) and biomass burning ($20.1 \pm 7.9\%$).

The rBC mass size distribution for the ensemble of all samples was monomodal and lognormal, and it had a MMD of 207 nm, which presumably was the result of the mixed emissions from the traffic, coal burning, biomass burning, and possibly other sources. The MMD for rBC from coal burning was 215 nm, which was ~26 nm larger than the MMD for the traffic source samples (189 nm). This difference can be attributed to

the combined effects of the fuel types burned, combustion conditions, transport, and aging. The results reported here are the first to document larger rBC particles in ambient air from coal burning compared with those from traffic sources from China. Furthermore, the number fraction of thickly coated rBC (f_{BC}) was much larger for the coal burning sample group (50.3 ± 7.7%) compared with the traffic source group (36.9 ± 7.2%). The contributions of organics, sulfate, and nitrate to the coatings on rBC from coal burning were estimated to be 44.0%, 32.3%, and 23.7%, respectively. In comparison, the contributions to the coatings of traffic rBC were organics = 63.2%, sulfate = 10.3%, and nitrate = 26.5%. These differences among the coatings from the two sources can be attributed to the complex processes involved in the formation of the rBC particles as well as those involved in the aging processes (condensation, coagulation, and photochemical oxidation) that alter the particles' size, composition, and mixing state after emission. These observations also imply that the rBC particles from coal burning will more readily act as cloud condensation nuclei than those from the traffic sources because the former have more hygroscopic (water-soluble ion) coatings.

High correlations (r = 0.78–0.83) were found between the rBC concentrations and CO mixing ratios, indicating that the two substances originated from the same or related sources. The overall rBC/ΔCO ratio determined from a robust linear regression was 5.9 μg m^{-3} ppm^{-1}, with ratios of 4.5 μg m^{-3} ppm^{-1} for the coal burning source and 2.7 μg m^{-3} ppm^{-1} for the traffic source. Based on the observed relationship between rBC and CO, one would estimate that roughly 4.5 Gg of rBC is emitted during winter in Xi'an. The TUV model indicated that the mean daytime value for the clear-sky DRF caused by rBC varied from −116.8 to −10.3 W m^{-2} and averaged −47.7 ± 28.9 W m^{-2}. Furthermore, rBC contributed 45.7% to the total surface atmospheric aerosol forcing of −100.5 ± 46.1 W m^{-2}. The mean daytime values for the total aerosol and rBC surface DRF during pollution periods (−107.4 and −49.3 W m^{-2}, respectively) were much higher than those during nonpollution periods (−59.3 W m^{-2} for total aerosol and −37.8 W m^{-2} for rBC), which was simply due to the larger particulate loadings during pollution periods.

Acknowledgments

This study was supported by the National Natural Science Foundation of China (41230641 and 41503118) and projects from the "Strategic Priority Research Program" of the Chinese Academy of Science (grants XDB05060500 and XDA05100401) and the Shaanxi Government (2012KTZB03-01-01 and 2011KTCQ03-04). The authors would like to thank Qiang Zhang from Tsinghua University for providing the CO emission inventory of Xi'an and three anonymous reviewers for their helpful comments on the manuscript. Data used in this study are available upon request from corresponding author at cao@loess.llqg.ac.cn.

References

Baumgardner, D., G. Kok, and G. Raga (2007), On the diurnal variability of particle properties related to light absorbing carbon in Mexico City, *Atmos. Chem. Phys.*, *7*(10), 2517–2526.

Bond, T. C., and R. W. Bergstrom (2006), Light absorption by carbonaceous particles: An investigative review, *Aerosol Sci. Technol.*, *40*(1), 27–67.

Bond, T. C., et al. (2013), Bounding the role of black carbon in the climate system: A scientific assessment, *J. Geophys. Res. Atmos.*, *118*, 5380–5552, doi:10.1002/jgrd.50171.

Cao, J., H. Xu, Q. Xu, B. Chen, and H. Kan (2012a), Fine particulate matter constituents and cardiopulmonary mortality in a heavily polluted Chinese city, *Environ. Health Perspect.*, *120*(3), 373–378.

Cao, J., Q. Y. Wang, J. C. Chow, J. G. Watson, X. X. Tie, Z. X. Shen, P. Wang, and Z. S. An (2012b), Impacts of aerosol compositions on visibility impairment in Xi'an, China, *Atmos. Environ.*, *59*, 559–566.

Cao, J. J., et al. (2007), Spatial and seasonal distributions of carbonaceous aerosols over China, *J. Geophys. Res.*, *112*, D22S11, doi:10.1029/2006JD008205.

Cao, J. J., C. S. Zhu, J. C. Chow, J. G. Watson, Y. M. Han, G. H. Wang, Z. X. Shen, and Z. S. An (2009), Black carbon relationships with emissions and meteorology in Xi'an, China, *Atmos. Res.*, *94*(2), 194–202.

Chen, L.-W. A., D. H. Lowenthal, J. G. Watson, D. Koracin, N. Kumar, E. M. Knipping, N. Wheeler, K. Craig, and S. Reid (2010), Toward effective source apportionment using positive matrix factorization: Experiments with simulated $PM_{2.5}$ data, *J. Air Waste Manage.*, *60*, 43–54.

Cheng, Y., K. B. He, F. K. Duan, M. Zheng, Y. L. Ma, J. H. Tan, and Z. Y. Du (2010), Improved measurement of carbonaceous aerosol: Evaluation of the sampling artifacts and inter-comparison of the thermal-optical analysis methods, *Atmos. Chem. Phys.*, *10*(17), 8533–8548.

Cheng, Y., G. Engling, K. B. He, F. K. Duan, Y. L. Ma, Z. Y. Du, J. M. Liu, M. Zheng, and R. J. Weber (2013), Biomass burning contribution to Beijing aerosol, *Atmos. Chem. Phys.*, *13*(15), 7765–7781.

Cuccia, E., D. Massabò, V. Ariola, M. Bove, P. Fermo, A. Piazzalunga, and P. Prati (2013), Size-resolved comprehensive characterization of airborne particulate matter, *Atmos. Environ.*, *67*, 14–26.

Dickerson, R., M. Andreae, T. Campos, O. Mayol-Bracero, C. Neususess, and D. Streets (2002), Analysis of black carbon and carbon monoxide observed over the Indian Ocean: Implications for emissions and photochemistry, *J. Geophys. Res.*, *107*(D19), 8017, doi:10.1029/2001JD000501.

Dubovik, O., A. Smirnov, B. Holben, M. King, Y. Kaufman, T. Eck, and I. Slutsker (2000), Accuracy assessments of aerosol optical properties retrieved from Aerosol Robotic Network (AERONET) Sun and sky radiance measurements, *J. Geophys. Res.*, *105*, 9791–9806, doi:10.1029/2000JD900040.

Eck, T. F., B. N. Holben, J. S. Reid, O. Dubovik, A. Smirnov, N. T. O'Neill, I. Slutsker, and S. Kinne (1999), Wavelength dependence of the optical depth of biomass burning, urban, and desert dust aerosols, *J. Geophys. Res.*, *104*, 31,333–31,349, doi:10.1029/1999JD900923.

Feng, J., M. Zhong, B. Xu, Y. Du, M. Wu, H. Wang, and C. Chen (2014), Concentrations, seasonal and diurnal variations of black carbon in $PM_{2.5}$ in Shanghai, China, *Atmos. Res.*, *147*, 1–9.

Gao, R., J. Schwarz, K. Kelly, D. Fahey, L. Watts, T. Thompson, J. Spackman, J. Slowik, E. Cross, and J.-H. Han (2007), A novel method for estimating light-scattering properties of soot aerosols using a modified single-particle soot photometer, *Aerosol Sci. Technol.*, *41*(2), 125–135.

Gysel, M., M. Laborde, J. Olfert, R. Subramanian, and A. Gröhn (2011), Effective density of Aquadag and fullerene soot black carbon reference materials used for SP2 calibration, *Atmos. Meas. Tech.*, *4*(12), 2851–2858.

Gysel, M., M. Laborde, A. Mensah, J. Corbin, A. Keller, J. Kim, A. Petzold, and B. Sierau (2012), Technical note: The single particle soot photometer fails to reliably detect PALAS soot nanoparticles, *Atmos. Meas. Tech.*, *5*(12), 3099–3107.

Han, S., et al. (2009), Temporal variations of elemental carbon in Beijing, *J. Geophys. Res.*, *114*, D23202, doi:10.1029/2009JD012027.

Hess, M., P. Koepke, and I. Schult (1998), Optical properties of aerosols and clouds: The software package OPAC, *Bull. Am. Meteorol. Soc.*, *79*(5), 831–844.

Huang, R.-J., et al. (2014), High secondary aerosol contribution to particulate pollution during haze events in China, *Nature*, *514*(7521), 218–222, doi:10.1038/nature13774.

Huang, X.-F., T.-L. Sun, L.-W. Zeng, G.-H. Yu, and S.-J. Luan (2012a), Black carbon aerosol characterization in a coastal city in South China using a single particle soot photometer, *Atmos. Environ.*, *51*, 21–28.

Huang, X.-F., L.-Y. He, L. Xue, T.-L. Sun, L.-W. Zeng, Z.-H. Gong, M. Hu, and T. Zhu (2012b), Highly time-resolved chemical characterization of atmospheric fine particles during 2010 Shanghai World Expo, *Atmos. Chem. Phys.*, *12*, 4897–4907.

Huang, X.-F., L. Xue, X.-D. Tian, W.-W. Shao, T.-L. Sun, Z.-H. Gong, W.-W. Ju, B. Jiang, M. Hu, and L.-Y. He (2013), Highly time-resolved carbonaceous aerosol characterization in Yangtze River Delta of China: Composition, mixing state and secondary formation, *Atmos. Environ.*, *64*, 200–207.

Intergovernmental Panel on Climate Change (2013), *Climate Change 2013: The Physical Science Basis. Contribution of Working Group I to the Fifth Assessment Report of the Intergovernmental Panel on Climate Change*, edited by T. F. Stocker et al., Cambridge Univ. Press, Cambridge, U. K.

Janssen, N., G. Hoek, M. Simic-Lawson, P. Fischer, L. Van Bree, H. Ten Brink, M. Keuken, R. W. Atkinson, H. R. Anderson, and B. Brunekreef (2011), Black carbon as an additional indicator of the adverse health effects of airborne particles compared with PM_{10} and $PM_{2.5}$, *Environ. Health Perspect.*, *119*(12), 1691–1699.

Kondo, Y., et al. (2006), Temporal variations of elemental carbon in Tokyo, *J. Geophys. Res.*, *111*, D12205, doi:10.1029/2005JD006257.

Laborde, M., P. Mertes, P. Zieger, J. Dommen, U. Baltensperger, and M. Gysel (2012), Sensitivity of the single particle soot photometer to different black carbon types, *Atmos. Meas. Tech.*, *5*, 1031–1043.

Li, Z., P. Goloub, O. Dubovik, L. Blarel, W. Zhang, T. Podvin, A. Sinyuk, M. Sorokin, H. Chen, and B. Holben (2009), Improvements for ground-based remote sensing of atmospheric aerosol properties by additional polarimetric measurements, *J. Quant. Spectros. Radiat. Transfer*, *110*(17), 1954–1961.

Liu, D., J. Allan, D. Young, H. Coe, D. Beddows, Z. Fleming, M. Flynn, M. Gallagher, R. Harrison, and J. Lee (2014), Size distribution, mixing state and source apportionment of black carbon aerosol in London during wintertime, *Atmos. Chem. Phys.*, *14*(18), 10,061–10,084.

Madronich, S. (1993), UV radiation in the natural and perturbed atmosphere, in *Environmental Effects of UV (Ultraviolet) Radiation*, edited by M. Tevini, pp. 17–69, Lewis Publisher, Boca Raton, Fla.

McMeeking, G., T. Hamburger, D. Liu, M. Flynn, W. Morgan, M. Northway, E. Highwood, R. Krejci, J. Allan, and A. Minikin (2010), Black carbon measurements in the boundary layer over western and northern Europe, *Atmos. Chem. Phys.*, *10*(19), 9393–9414.

McMeeking, G., W. Morgan, M. Flynn, E. Highwood, K. Turnbull, J. Haywood, and H. Coe (2011), Black carbon aerosol mixing state, organic aerosols and aerosol optical properties over the United Kingdom, *Atmos. Chem. Phys.*, *11*(17), 9037–9052.

Metcalf, A., J. Craven, J. Ensberg, J. Brioude, W. Angevine, A. Sorooshian, H. Duong, H. Jonsson, R. Flagan, and J. Seinfeld (2012), Black carbon aerosol over the Los Angeles Basin during CalNex, *J. Geophys. Res.*, *117*, D00V13, doi:10.1029/2011JD017255.

Miconnet, N., A. H. Geeraerd, J. F. Van Impe, L. Rosso, and M. Cornu (2005), Reflections on the use of robust and least-squares non-linear regression to model challenge tests conducted in/on food products, *Int. J. Food Microbiol.*, *104*(2), 161–177.

Moffet, R. C., and K. A. Prather (2009), In-situ measurements of the mixing state and optical properties of soot with implications for radiative forcing estimates, *Proc. Natl. Acad. Sci. U.S.A.*, *106*(29), 11,872–11,877.

Moteki, N., and Y. Kondo (2007), Effects of mixing state on black carbon measurements by laser-induced incandescence, *Aerosol Sci. Technol.*, *41*(4), 398–417.

Moteki, N., and Y. Kondo (2010), Dependence of laser-induced incandescence on physical properties of black carbon aerosols: Measurements and theoretical interpretation, *Aerosol Sci. Technol.*, *44*(8), 663–675.

Ng, N. L., S. C. Herndon, A. Trimborn, M. R. Canagaratna, P. Croteau, T. B. Onasch, D. Sueper, D. R. Worsnop, Q. Zhang, and Y. Sun (2011), An Aerosol Chemical Speciation Monitor (ACSM) for routine monitoring of the composition and mass concentrations of ambient aerosol, *Aerosol Sci. Technol.*, *45*(7), 780–794.

Orasche, J., J. Schnelle-Kreis, G. Abbaszade, and R. Zimmermann (2011), Technical note: In-situ derivatization thermal desorption GC-TOFMS for direct analysis of particle-bound non-polar and polar organic species, *Atmos. Chem. Phys.*, *11*(17), 8977–8993.

Paatero, P., and U. Tapper (1994), Positive matrix factorization: A non-negative factor model with optimal utilization of error estimates of data values, *Environmetrics*, *5*(2), 111–126.

Petzold, A., et al. (2013), Recommendations for reporting "black carbon" measurements, *Atmos. Chem. Phys.*, *13*(16), 8365–8379.

Polissar, A. V., P. K. Hopke, P. Paatero, W. C. Malm, and J. F. Sisler (1998), Atmospheric aerosol over Alaska: 2. Elemental composition and sources, *J. Geophys. Res.*, *103*, 19,045–19,057, doi:10.1029/98JD01212.

Rutter, A. P., D. C. Snyder, J. J. Schauer, J. DeMinter, and B. Shelton (2009), Sensitivity and bias of molecular marker-based aerosol source apportionment models to small contributions of coal combustion soot, *Environ. Sci. Technol.*, *43*(20), 7770–7777.

Schwarz, J. P., et al. (2006), Single-particle measurements of midlatitude black carbon and light-scattering aerosols from the boundary layer to the lower stratosphere, *J. Geophys. Res.*, *111*, D16207, doi:10.1029/2006JD007076.

Schwarz, J. P., et al. (2008), Measurement of the mixing state, mass, and optical size of individual black carbon particles in urban and biomass burning emissions, *Geophys. Res. Lett.*, *35*, L13810, doi:10.1029/2008GL033968.

Schwarz, J. P., J. Spackman, R. Gao, A. Perring, E. Cross, T. Onasch, A. Ahern, W. Wrobel, P. Davidovits, and J. Olfert (2010), The detection efficiency of the single particle soot photometer, *Aerosol Sci. Technol.*, *44*(8), 612–628.

Sheehan, P., E. Cheng, A. English, and F. Sun (2014), China's response to the air pollution shock, *Nat. Clim. Change*, *4*(5), 306–309, doi:10.1038/nclimate2197.

Shindell, D., J. C. Kuylenstierna, E. Vignati, R. van Dingenen, M. Amann, Z. Klimont, S. C. Anenberg, N. Muller, G. Janssens-Maenhout, and F. Raes (2012), Simultaneously mitigating near-term climate change and improving human health and food security, *Science*, *335*(6065), 183–189.

Shiraiwa, M., Y. Kondo, N. Moteki, N. Takegawa, Y. Miyazaki, and D. Blake (2007), Evolution of mixing state of black carbon in polluted air from Tokyo, *Geophys. Res. Lett.*, *34*, L16803, doi:10.1029/2007GL029819.

Slowik, J. G., K. Stainken, P. Davidovits, L. Williams, J. Jayne, C. Kolb, D. R. Worsnop, Y. Rudich, P. F. DeCarlo, and J. L. Jimenez (2004), Particle morphology and density characterization by combined mobility and aerodynamic diameter measurements. Part 2: Application to combustion-generated soot aerosols as a function of fuel equivalence ratio, *Aerosol Sci. Technol.*, *38*(12), 1206–1222.

Slowik, J. G., A. Vlasenko, M. McGuire, G. J. Evans, and J. P. D. Abbatt (2010), Simultaneous factor analysis of organic particle and gas mass spectra: AMS and PTR-MS measurements at an urban site, *Atmos. Chem. Phys.*, *10*, 1969–1988.

Spackman, J., J. Schwarz, R. Gao, L. Watts, D. Thomson, D. Fahey, J. Holloway, J. de Gouw, M. Trainer, and T. Ryerson (2008), Empirical correlations between black carbon aerosol and carbon monoxide in the lower and middle troposphere, *Geophys. Res. Lett.*, *35*, L19816, doi:10.1029/2008GL035237.

Su, X., J. Cao, Z. Li, M. Lin, and G. Wang (2014), Column-integrated aerosol optical properties during summer and autumn of 2012 in Xi'an, China, *Aerosol Air Qual. Res.*, *14*(3), 850–861.

Subramanian, R., G. Kok, D. Baumgardner, A. Clarke, Y. Shinozuka, T. Campos, C. Heizer, B. Stephens, B. De Foy, and P. Voss (2010), Black carbon over Mexico: The effect of atmospheric transport on mixing state, mass absorption cross-section, and BC/CO ratios, *Atmos. Chem. Phys.*, *10*(1), 219–237.

Tian, H., K. Liu, J. Zhou, L. Lu, J. Hao, P. Qiu, J. Gao, C. Zhu, K. Wang, and S. Hua (2014), Atmospheric emission inventory of hazardous trace elements from China's coal-fired power plants—Temporal trends and spatial variation characteristics, *Environ. Sci. Technol.*, *48*(6), 3575–3582.

Tie, X., and J. Cao (2009), Aerosol pollution in China: Present and future impact on environment, *Particuology*, *7*(6), 426–431.

Verma, R., L. Sahu, Y. Kondo, N. Takegawa, S. Han, J. Jung, Y. Kim, S. Fan, N. Sugimoto, and M. Shammaa (2010), Temporal variations of black carbon in Guangzhou, China, in summer 2006, *Atmos. Chem. Phys.*, *10*(14), 6471–6485.

Wang, Q., J. Cao, J. Tao, N. Li, X. Su, L. A. Chen, P. Wang, Z. Shen, S. Liu, and W. Dai (2013), Long-term trends in visibility and at Chengdu, China, *PLoS One*, *8*, e68894, doi:10.1371/journal.pone.0068894.

Wang, Q., J. Schwarz, J. Cao, R. Gao, D. Fahey, T. Hu, R.-J. Huang, Y. Han, and Z. Shen (2014a), Black carbon aerosol characterization in a remote area of Qinghai-Tibetan Plateau, western China, *Sci. Total Environ.*, *479*, 151–158.

Wang, Q., R.-J. Huang, J. Cao, Y. Han, G. Wang, G. Li, Y. Wang, W. Dai, R. Zhang, and Y. Zhou (2014b), Mixing state of black carbon aerosol in a heavily polluted urban area of China: Implications for light absorption enhancement, *Aerosol Sci. Technol.*, *48*(7), 689–697.

Wang, Q. Y., et al. (2015), Black carbon aerosol in winter northeastern Qinghai–Tibetan Plateau, China: The source, mixing state and optical property, *Atmos. Chem. Phys.*, *15*, 13,059–13,069.

Wild, M., A. Ohmura, and K. Makowski (2007), Impact of global dimming and brightening on global warming, *Geophys. Res. Lett.*, *34*, L04702, doi:10.1029/2006GL028031.

Wu, D., C. Wu, B. Liao, H. Chen, M. Wu, F. Li, H. Tan, T. Deng, H. Li, and D. Jiang (2013), Black carbon over the South China Sea and in various continental locations in South China, *Atmos. Chem. Phys.*, *13*(24), 12,257–12,270.

Wu, Y., R. Zhang, P. Tian, J. Tao, S. C. Hsu, P. Yan, Q. Wang, J. Cao, X. Zhang, and X. Xia (2016), Effect of ambient humidity on the light absorption amplification of black carbon in Beijing during January 2013, *Atmos. Environ.*, *124*(Part B), 217–223.

Xia, X., Z. Li, P. Wang, H. Chen, and M. Cribb (2007a), Estimation of aerosol effects on surface irradiance based on measurements and radiative transfer model simulations in northern China, *J. Geophys. Res.*, *112*, D22S10, doi:10.1029/2006JD008337.

Xia, X., Z. Li, B. Holben, P. Wang, T. Eck, H. Chen, M. Cribb, and Y. Zhao (2007b), Aerosol optical properties and radiative effects in the Yangtze Delta region of China, *J. Geophys. Res.*, *112*, D22S12, doi:10.1029/2007JD008859.

Xiao, S., Q. Wang, J. Cao, R.-J. Huang, W. Chen, Y. Han, H. Xu, S. Liu, Y. Zhou, and P. Wang (2014), Long-term trends in visibility and impacts of aerosol composition on visibility impairment in Baoji, China, *Atmos. Res.*, *149*, 88–95.

Xu, B., J. Cao, J. Hansen, T. Yao, D. R. Joswia, N. Wang, G. Wu, M. Wang, H. Zhao, and W. Yang (2009), Black soot and the survival of Tibetan glaciers, *Proc. Natl. Acad. Sci. U.S.A.*, *106*(52), 22,114–22,118.

Xu, H., J. Cao, K. Ho, H. Ding, Y. Han, G. Wang, J. Chow, J. Watson, S. Khol, and J. Qiang (2012), Lead concentrations in fine particulate matter after the phasing out of leaded gasoline in Xi'an, China, *Atmos. Environ.*, *46*, 217–224.

Xu, J., M. H. Bergin, R. Greenwald, and P. B. Russell (2003), Direct aerosol radiative forcing in the Yangtze delta region of China: Observation and model estimation, *J. Geophys. Res.*, *108*(D2), 4060, doi:10.1029/2002JD002550.

Zechmeister, H. G., D. Hohenwallner, A. Riss, and A. Hanus-Illnar (2005), Estimation of element deposition derived from road traffic sources by using mosses, *Environ. Pollut.*, *138*(2), 238–249.

Zhang, Q., D. G. Streets, G. R. Carmichael, K. He, H. Huo, A. Kannari, Z. Klimont, I. Park, S. Reddy, and J. Fu (2009), Asian emissions in 2006 for the NASA INTEX-B mission, *Atmos. Chem. Phys.*, *9*(14), 5131–5153.

Zhang, T., J. Cao, X. Tie, Z. Shen, S. Liu, H. Ding, Y. Han, G. Wang, K. Ho, and J. Qiang (2011), Water-soluble ions in atmospheric aerosols measured in Xi'an, China: Seasonal variations and sources, *Atmos. Res.*, *102*(1), 110–119.

Zhang, T., J.-J. Cao, J. C. Chow, Z.-X. Shen, K.-F. Ho, S. S. H. Ho, S.-X. Liu, Y.-M. Han, J. G. Watson, and G.-H. Wang (2014), Characterization and seasonal variations of levoglucosan in fine particulate matter in Xi'an, China, *J. Air Waste Manage. Assoc.*, *64*(11), 1317–1327.

Zhang, X. Y., Y. Q. Wang, X. Zhang, W. Guo, and S. L. Gong (2008), Carbonaceous aerosol composition over various regions of China during 2006, *J. Geophys. Res.*, *113*, D14111, doi:10.1029/2007JD009525.

Zhang, Y.-L., R.-J. Huang, I. El Haddad, K.-F. Ho, J.-J. Cao, Y. Han, P. Zotter, C. Bozzetti, K. Daellenbach, and F. Canonaco (2015), Fossil vs. non-fossil sources of fine carbonaceous aerosols in four Chinese cities during the extreme winter haze episode of 2013, *Atmos. Chem. Phys.*, *15*(3), 1299–1312.

Zhuang, B., T. Wang, J. Liu, S. Li, M. Xie, X. Yang, C. Fu, J. Sun, C. Yin, and J. Liao (2014), Continuous measurement of black carbon aerosol in urban Nanjing of Yangtze River Delta, China, *Atmos. Environ.*, *89*, 415–424.